RESEARCH ARTICLE

The importance of local process conditions on the properties of fused filament fabrication printed polypropylene components

Yao Xu[1] | **Miaozi Huang[1]** | **Alois K. Schlarb[1,2,3]** ⓘ

[1]Chair of Composite Engineering (CCe), Rheinland-Pfälzische Technische Universität (RPTU), Kaiserslautern, Germany

[2]Research Center OPTIMAS, Rheinland-Pfälzische Technische Universität (RPTU), Kaiserslautern, Germany

[3]Key Lab of Rubber-Plastics, Qingdao University of Science and Technology, Qingdao, China

Correspondence
Alois K. Schlarb, Chair of Composite Engineering (CCe), Rheinland-Pfälzische Technische Universität (RPTU), Gottlieb-Daimler-Str. Bld. 44 67663 Kaiserslautern, Germany.
Email: alois.schlarb@mv.uni-kl.de

Abstract

A key characteristic of the manufacture of void free components by 3D printing using fused filament fabrication (FFF) is that this generative process always produces new welded joints between the hot strand leaving the nozzle and the previously deposited and already solidified area. These contact conditions determine the local temperature gradient and the local deformation gradients in the contact. These in turn can have a decisive effect on the morphology and mechanical behavior of the component. In this work, the influence of three different geometric contact conditions under two different machine parameter sets on the morphology and mechanical properties was investigated. The results show that ultimately a parameter simply calculated from the process settings and geometric boundary conditions, the mean contact temperature, is decisive for the properties of the component. If this value is above the melting temperature of the material, quasi-homogeneous morphologies with decent mechanical properties can be achieved in any case. However, if the mean contact temperature is below the melting temperature, the deformation conditions during strand deposition have a significant influence on morphology and properties. The paper describes this behavior using the example of three contact geometries typically encountered in 3D printing with FFF. The discussed correlations between the morphology and the mechanical properties of the printed FFF samples lead to a better understanding of the process and ultimately to the conclusion that the path generation that is, the slicing strategy should take these facts into account in the future in order to be able to exploit the material-intrinsic performance potential in 3D printing as well.

KEYWORDS
fused filament fabrication, interlayer strength, morphology, polypropylene

1 | INTRODUCTION

Additive manufacturing (AM) is able to obtain extremely complex geometries in a single process, thus providing a great degree of freedom in the design.[1–3] Fused filament fabrication (FFF) as one of AM processes was prevalent due to its simplicity and lower cost. In the FFF process, the material filament is fed into a printer via a pinch-roller mechanism. During the extrusion process, the filament melts and is extruded through a nozzle, with the solid portion of the filament acting as a piston to push the melt along the nozzle. Three-dimensional objects are built layer upon layer via material delivery along defined paths. A lot of commercially polymeric materials can be used to print components for academic and industrial applications with the development of the FFF.[4–8] As one of the semi-crystalline thermoplastics, isotactic polypropylene (PP) has increasingly attracted attention for FFF due to its excellent properties and widespread commercial use.[9–12]

The properties of the 3D printed part were affected by different factors, such as infill pattern,[13] printing speed,[14] and nozzle temperature.[15] Various studies have been conducted to enhance the mechanical properties of FFF parts by reducing void content in recent years.[16–21] But even for components without voids, the mechanical properties are significantly influenced by the morphology of the weld lines.[10] During the formation of the welding line, the strand comes into physical contact with adjacent strands, simultaneously transferring thermal energy to the adjacent strand.[22] For semi-crystalline polymers, while cooling, the crystallization process and inter-diffusion between the strands take place simultaneously. It is generally accepted that the mobility of polymer chains is drastically reduced upon crystallization, as the polymer chains are embedded in the growing crystals. Consequently, it is pivotal to establish sufficiently strong interlayer bonds that the deposited strand be maintained above the crystallization temperature for an adequate time to allow molecular diffusion.[10] In contrast to conventional fabrication, the printed parts are far from homogeneous due to the local flow condition and thermal gradients.[15,17,18] The complex features of the FFF, especially the local conditions during the formation of the welding line, such as thermal history[23–25] and shear stress,[26] play a vital role in the final properties of the components. The interfacial bonding between the adjacent strands is thermally driven and affects the morphology and ultimately the mechanical properties.[27,28]

In addition to thermal conditions, local flow processes during the processing of thermoplastics have a significant effect on the structure formation, morphology and mechanical properties of components produced in this way.[29] Thus, in FFF, local deformations/flow movements take place in all three spatial directions during the depositing process in material contact with the neighboring material areas. These deformations affect the morphological formation of the contact areas that is, ultimately the component quality perpendicular to the printing direction. Basically, three classic contact cases can be distinguished in 3D printing with FFF and 100% infill.

1. Case "Wall" (W): The currently deposited strand is in contact with the layer below it only on its underside.
2. Case "Fillet" (F): The currently deposited strand has contact on its underside with the layer below and on one flank with the neighboring strand in the same layer (Comparable to a fillet weld in extrusion welding).
3. Case "Groove" (G): The currently deposited strand has contact on its bottom side to the layer below and on both flanks contact with the neighboring strands in the same layer.

However, how these different cases affect the local deformation behavior and thus the joint quality has hardly been investigated in the literature so far. The objective of the present work was to investigate the effects of three different types of geometric contact typical for the FFF process during the printing process on morphology and mechanical properties. Therefore, in this work, we have focused specifically on the properties of a component perpendicular to the printing direction. For this purpose, we have systematically varied the process and contact conditions (cases W, F, and G) in a practical manner. The analysis of the supermolecular morphology and the quantification of the strength properties using microtensile tests are the experimental basis for our conclusions.

2 | MATERIALS AND METHODS

Isotactic polypropylene (PP) HD120MO from Borealis GmbH, Burghausen, was used in this study. The PP filaments with a diameter of 2.8 ± 0.05 mm were extruded through a single-screw extruder (EX6, Filabot, Barre, USA). The same processing conditions used in a previous work[22] were used to produce the filaments. Screw speed was set at 6 rpm and barrel temperatures at 40/130/200/195°C.

The final samples were produced with a 3D printer (Ultimaker 3, Ultimaker B.V., Netherlands). A nozzle temperature of 230°C, a platform temperature of 80°C, a layer height of 0.1 mm and a printing speed of 10 mm/s were selected. The nozzle diameter was 0.4 mm. With

$L = 50$ mm and $L = 5$ mm, two different sample lengths were produced. The lengths were chosen to obtain two different contact temperature situations, $T_c < T_m$ and $T_c > T_m$. The contact temperatures of the printed specimens in the symmetry plane A-A determined according to a previous work[22] are listed in the supplement. The print paths were chosen so that three contact geometries could be set, which are typical for the production of compact components with 100% filling in the FFF process, as shown in Figure 1.

In case W, the walls were printed in (deformed) strand width, as is typical when printing the outline of a component. In case F, the strands were applied in a meandering pattern in each layer, as is common when printing parts with 100% infill. In case G, the last strand in each layer was applied in a groove. The time sequence for the production of the specimens is shown schematically in the online appendix.

The supermolecular morphology of the samples was analyzed using a 3D laser scanning microscope (LSM) (VK-X1050, Keyence GmbH, Japan) in the section plane AA (Figure 2a). For this purpose, a rotating microtome (Hyrax M 25, Carl Zeiss Microlmaging GmbH, Jena, Germany) was first used to create a smooth surface, which was then chemically etched as described in detail in a previous work.[10]

The thermal properties of the samples were characterized using a differential scanning calorimeter (DSC Q20, TA Instruments, USA). The heating rate was 10°C/min from 30 to 200°C. The degree of crystallization X_m was determined from the measured melting enthalpy ΔH_m by diffusion with the value for PP of $\Delta H_m = 207$ J/g known from literature[30]:

$$X_m = \frac{\Delta H_m}{\Delta H_m^0} \times 100\%. \tag{1}$$

In order to be able to draw conclusions about the thermal/mechanical contact conditions during printing via the recrystallization behavior, thin sections with a thickness of 30 μm in the yz plane were taken from the specimens, and heated in a hot stage (Linkam LTS420, Surrey,

England) under a polarizing microscope (ECLIPSE LV100, Nikon GmbH, Düsseldorf, Germany) at a heating rate of 20°C/min from room temperature to 178°C, held there for 10 min, and then cooled to room temperature at a rate of 10°C/min. As shown by earlier studies,[30–33] it is very likely that, due to the relatively low holding temperature of 178°C, stable structures formed by local melt deformation and cooling processes do not melt completely. It is precisely at these points that the first supermolecular structures detectable by polarization optics appear when the thin section is cooled.

To prepare the tensile specimens, 30 μm thick thin sections were taken from the section plane BB of specimens W, F, and G, respectively (Figure 2). The specimens were tested on a micro-tensile machine (Tension & Compression Module, Kammrath & Weiss GmbH, Dortmund, Germany) at a crosshead speed of 20 μm/s in the z-direction. The tensile force was recorded as a function of time. In parallel, the deformation process was recorded using an optical microscope with the charge-coupled device (CCD) camera. Stress–strain curves were calculated from the force/deformation value pairs, as well as the section xy-cross-section and the initial crosshead distance. Tests were repeated five times with the same conditions for each case in order to ensure consistency of results.

3 | RESULTS AND DISCUSSIONS

3.1 | Morphology

Figure 3a–c shows 3D laser scanning microscope images of section AA and the height profiles of the investigated contact geometries for the case $T_c < T_m$. Clearly, the contact geometries dominate the morphology of the samples. In all cases, the pattern of deposition that is, the demarcation between the strands, is well recognizable. The morphological differences are strongest in case G (Figure 3c) that is, the utmost influences on the mechanical behavior are to be expected here. Therefore, this case was also analyzed for $T_c > T_m$ (Figure 3d). A simplified
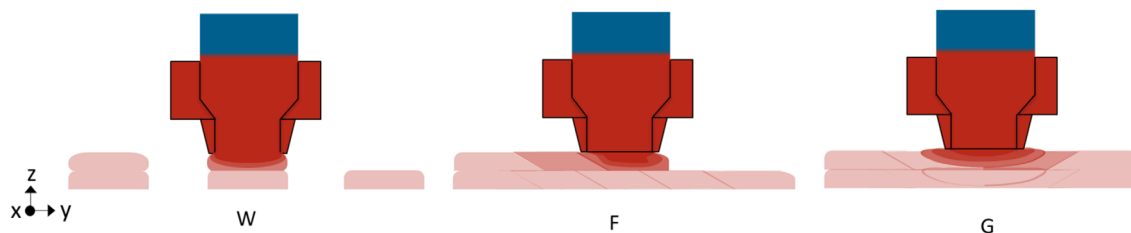

FIGURE 1 Contact geometries [Color figure can be viewed at wileyonlinelibrary.com]
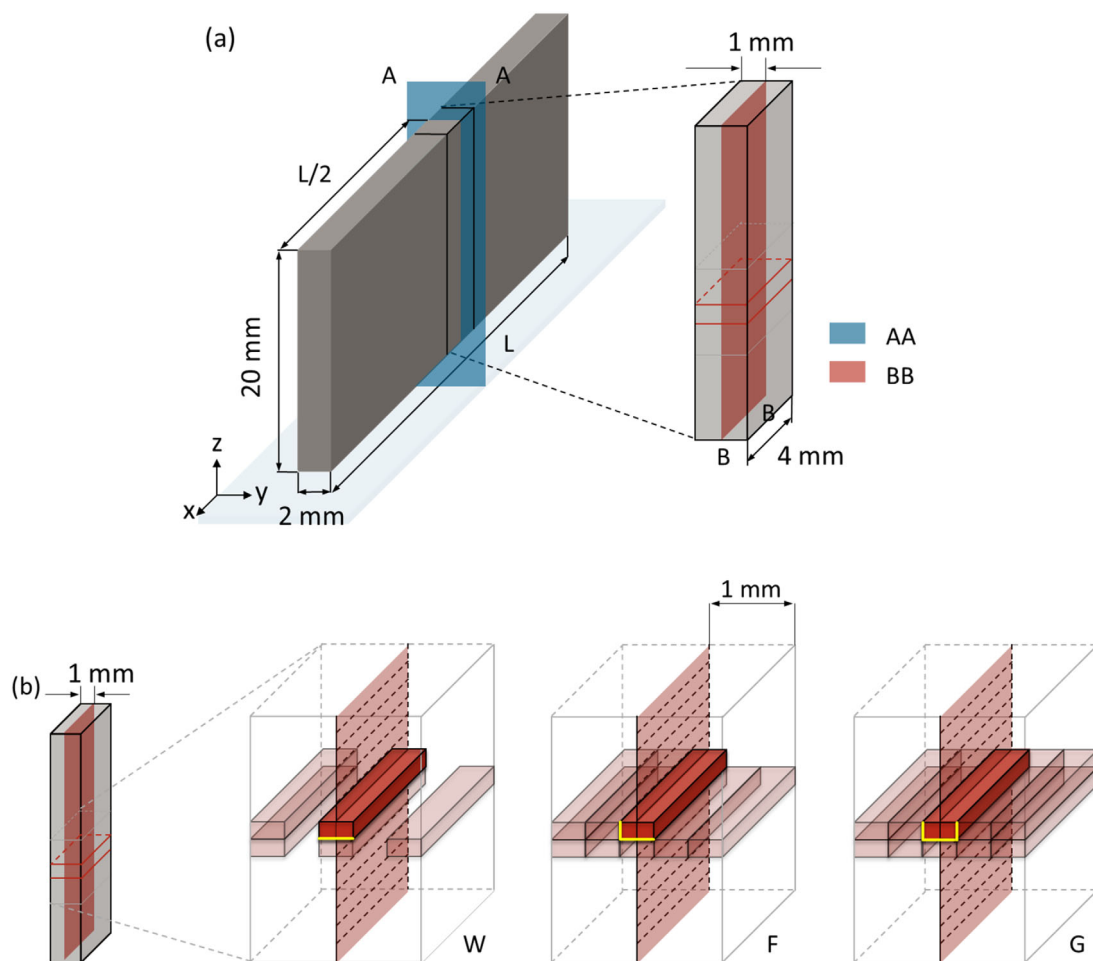
FIGURE 2 Schematic representation of sample preparation of (a) fused filament fabrication printed bar-shaped specimens and (b) the location of the thin sections for micro-tensile test are specified by the middle strand of specimen case W, F and G. [Color figure can be viewed at wileyonlinelibrary.com]

schematic representation is shown in Figure 3 for each case on the left. In the online appendix, the chronological sequence in the development of these cases is shown in more detail schematically.

In case W, the welds between the layers are the least pronounced, but as also shown by the height profile. Interestingly, in the height profile the contact line between the layers is below the reference plane. Since the etching process is more abrasive in regions with low near order of molecules, such as the amorphous regions,[34,35] the transition region also appears to be mechanically weaker. Spherulitic superstructures can be seen in the strand itself. As expected, the spherulite size decreases from the interior of the strand to the edge, which is due to the temperature gradient and associated locally different cooling rates.

In the contact case F, the strand cross sections deform into a rhomb. When leaving the nozzle, the melt relaxes, which leads to so-called die swelling.[28] At the same time, the possibility of deformation is hindered by the forming

constraint on one flank to the neighboring strand and on the underside by the underlying layer, which ultimately leads to a rhombus in the cross section. The height profile is more pronounced. The contact line appears to be significantly more resistant to attack by the etchant than in case W. Transcrystalline structures form from the contact line, which change into spherulitic structures inside the strand.

The strongest morphological differences between the individual layers can be seen in case G. Obviously, there is no longer sufficient volume available for the deposited mass to be placed in the groove largely without deformation. Instead, a complex flow field is formed here, which ultimately leads to an extremely different supermolecular structure during material interlock between the layers. However, when the contact temperature is above the melting temperature of the material, the demarcation between the strands is non-pronounced even at case G.

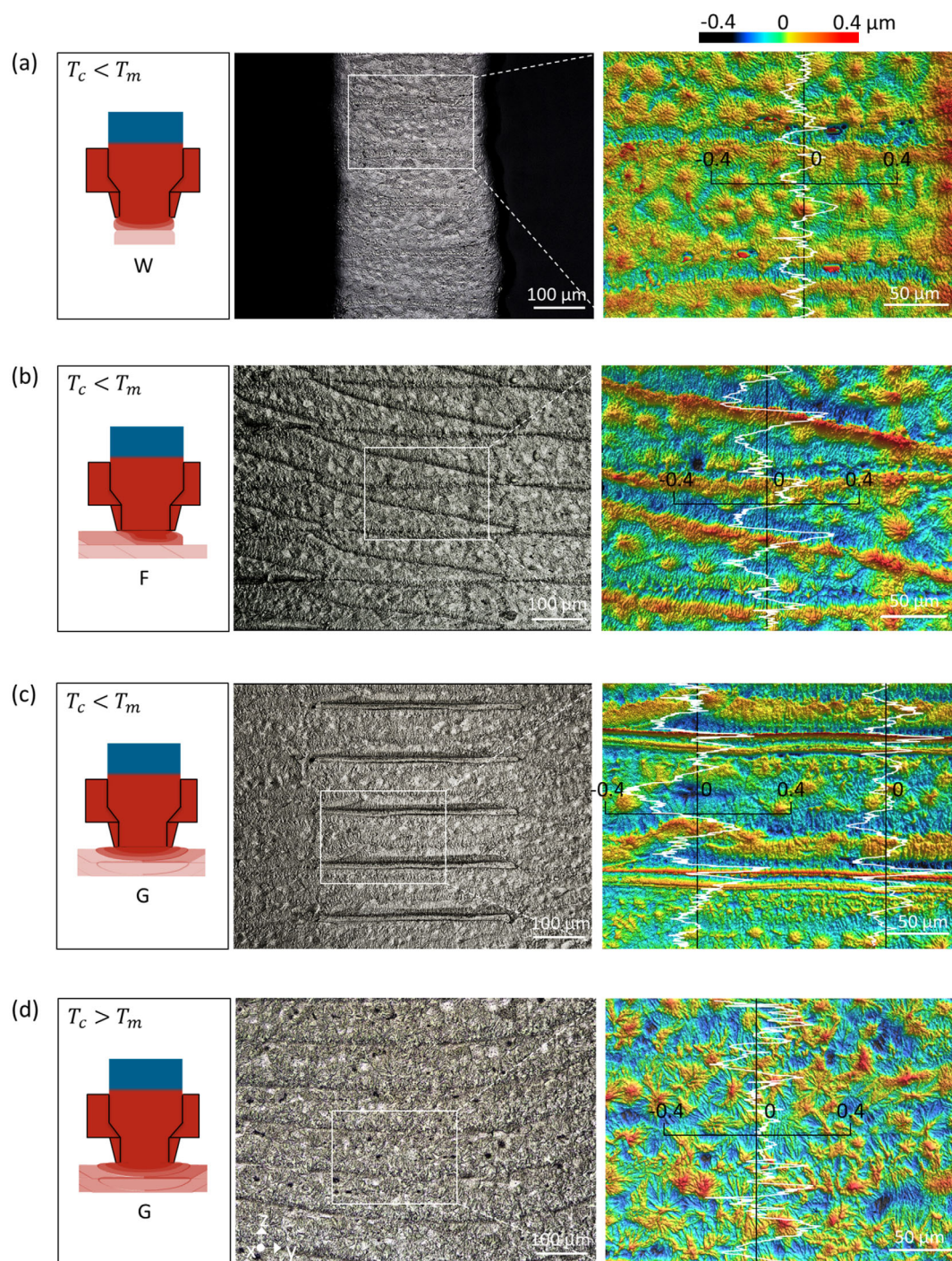The DSC curves of the first heating from the contact temperature condition $T_c < T_m$ in Figure 4 show the

FIGURE 3 Three-dimensional laser scanning microscope images of cross-section A–A at different contact situations, corresponding magnified images with color coded height information and corresponding height curves at the position of the black solid line. [Color figure can be viewed at wileyonlinelibrary.com]

same behavior for cases W and F, that is, one sees a melting peak at about 165°C, which corresponds to the alpha modification of polypropylene. The degree of crystallinity of the samples from these regions is almost identical. In case G, the alpha modification is also visible at 165°. In addition, however, the curve also shows a local maximum at 150°C, indicating the beta modification of polypropylene. At the same time, the degree of crystallinity is slightly higher compared to cases W and F.

Figure 5 shows the local evolution of the supramolecular structure during non-isothermal cooling in a highlight-like manner based on images taken at temperatures of $T = 130$, 120, and 110°C. The morphology formation is different in all three cases when the contact

temperature during printing was below the melting temperature.

The first signs of birefringence appear very clearly at 130°C in case G, exactly in the contact plane between the layers (see white arrows). For case F, the first morphological changes are only indicated by some darker spots in the melt. In contrast, the melt in case W showed no signs of birefringence that is, there are no structures visible under the light microscope.
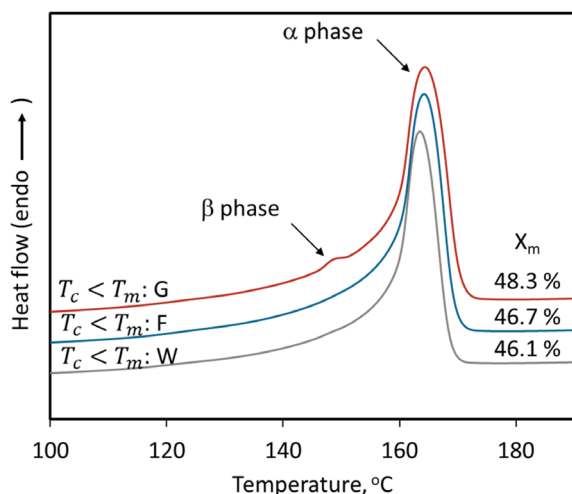

FIGURE 4 Differential scanning calorimetry curves of specimens taken from the different areas (case [W, F, G; $T_c < T_m$]). [Color figure can be viewed at wileyonlinelibrary.com]

At 120°C, on the other hand, supermolecular structures that is, essentially spherulites, are visible in all three cases. In case G, the spherulites between the layers have grown considerably. In addition, the diagonal contact areas between strands in a layer are now uniquely occupied by spherulites. Similarly, the diagonals in each layer in case F are largely represented by spherulites. In case W, spherulitic structures appear more abundantly in the specimen edge region. Inside the wall, however, spherulites are largely uniformly distributed.

At 100°C, all samples are almost completely occupied by supermolecular structures that is, crystallization is largely complete.

3.2 | Mechanical properties

The performance of microtensile tests on thin sections in the z-direction also shows clear differences for the three characteristic cases (Figure 6).

At a calculated contact temperature lower than the melting temperature, all characteristic values that is, yield stress, tensile strength and elongation at break, are highest in case W, followed by case F and finally case G. At a calculated contact temperature higher than the melting temperature, high strength values are also obtained in case G, but not quite the elongation values of W at low temperature. It is worth noting that the tensile strength of the specimens case W at low contact
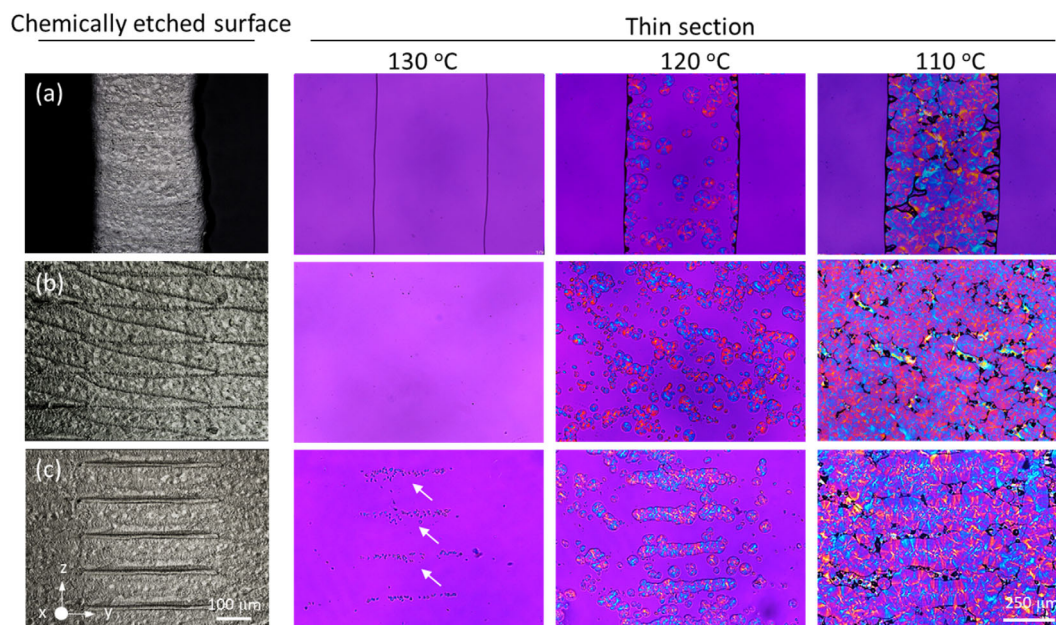

FIGURE 5 Micrographs of chemically etched surfaces (left) and development of supermolecular morphology during cooling in a hot stage; (a) represents case W, (b) case F, and (c) case G. [Color figure can be viewed at wileyonlinelibrary.com]
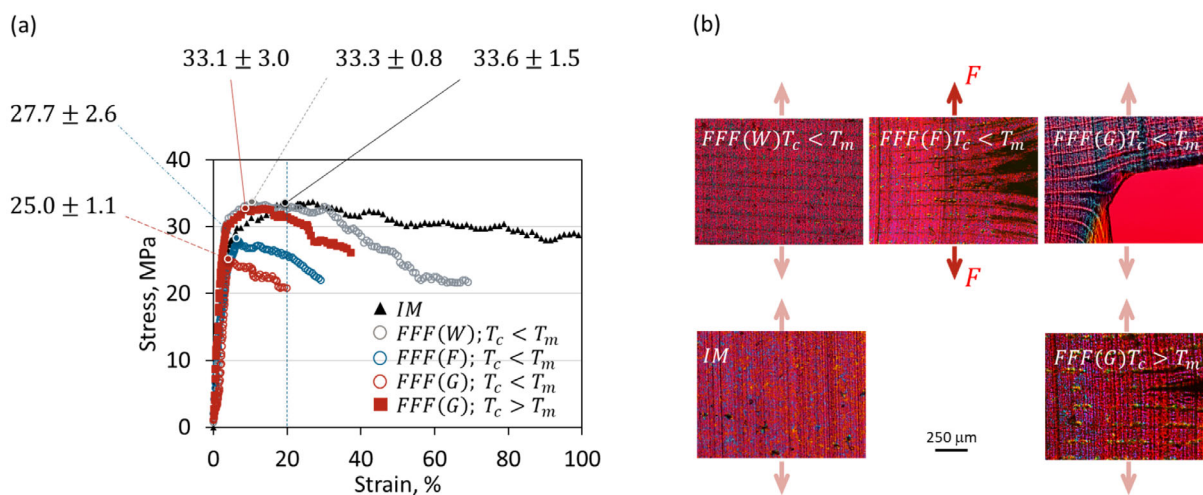
FIGURE 6 (a) Representative stress–strain curves obtained by the micro-tensile device and (b) the corresponded optical micrographs of the thin sections of IM specimen and FFF specimen of the different contact temperature and areas (case [W, F, G]) at elongation of 20% during tensile process. The red arrows indicate the direction of tensile force. [Color figure can be viewed at wileyonlinelibrary.com]

temperature and case G at high contact temperature reached the level of the injection molded (IM) PP.

Microscopically, it was found that locally higher deformations always occur in the contact areas between the layers that is, in the zone influenced by the welding process. The polarization microscopic images show that at a global strain of 20% at $T_c < T_m$ in case G a macro-crack has formed and finally failure occurs there.

4 | CONCLUSIONS

In this work, three typical contact geometries of void free FFF-printed specimens were investigated under two fundamentally different contact temperature conditions. The results show that the contact geometry has a significant influence on the local deformation during deposition and thus on the morphology and mechanical properties when the calculated contact temperature during layup is below the melting temperature of the material. A strand freely deposited on a layer deforms into an ellipse. If the hot strand is deposited next to an already cooled strand, comparable with a fillet weld during welding, the cross-section is roughly deformed into a rhombus. If the hot strand is deposited in a groove bounded by two already deposited strands, comparable with a U-seam in welding, this is accompanied by significantly higher local deformations. Specimens with lower local deformation during deposition exhibit an almost homogeneous morphology and less pronounced weld lines, resulting in mechanical properties comparable with injection molded specimens. In contrast, the strand deposited in a groove leads to clearly visible morphology gradients resulting in

significantly lower strength in the component. The evolution of the morphology observed in the optical microscope under polarized light shows that crystallization initially occurs along the weld line between the layers of the strand deposited in a groove. This indicates flow-induced local nucleation and the resulting anisotropic supermolecular morphology formation.

The structural mechanics investigations with thin sections in the optical microscope confirm that specimens produced with low local deformation deform largely uniformly under tensile load, then finally fail in a joint area by cracking under high global deformation. In these cases, the stiffness and strength of injection molded samples can be achieved. However, injection molded samples still show a higher elongation at break. Specimens produced under locally severe deformation show significantly larger strains in the fusion regions and significantly lower strengths at failure in these regions in the microtensile test, even at low global deformation.

As shown in the most critical case G, the morphological inhomogeneity disappears almost completely when the calculated contact temperature is higher than the melting temperature and at least the strength properties are at the data sheet level of the material manufacturer.

In a component printed with a common set of parameters, all these cases at different contact temperatures can occur at different positions in the component. It is therefore not surprising that it is precisely the homogeneity of 3D-printed components that remains a particular challenge to this day. The key to uniformly high component quality therefore lies in controlling the heat balance during the deposition process.

AUTHOR CONTRIBUTIONS

Yao Xu: Data curation (lead); investigation (lead); methodology (equal); visualization (equal); writing – original draft (equal). **Miaozi Huang:** Funding acquisition (supporting); methodology (equal); validation (equal); visualization (supporting); writing – original draft (supporting); writing – review and editing (supporting). **Alois K. Schlarb:** Conceptualization (lead); funding acquisition (lead); resources (lead); supervision (lead); visualization (equal); writing – review and editing (lead).

ACKNOWLEDGMENTS

CONFLICT OF INTEREST STATEMENT

The authors declare no conflict of interest.

DATA AVAILABILITY STATEMENT

The data that support the findings of this study are available on request from the corresponding author. The data are not publicly available due to privacy or ethical restrictions.

ORCID

Alois K. Schlarb https://orcid.org/0000-0001-8693-9163

REFERENCES

[1] A. C. Abbott, G. P. Tandon, R. L. Bradford, H. Koerner, J. W. Baur, *Addit. Manuf.* **2018**, *19*, 29.

[2] Y. Liao, C. Liu, B. Coppola, G. Barra, L. Di Maio, L. Incarnato, K. Lafdi, *Polymers* **2019**, *11*, 1.

[3] S. Petersmann, P. Spoerk-Erdely, M. Feuchter, T. Wieme, F. Arbeiter, M. Spoerk, *Addit. Manuf.* **2020**, *35*, 101384.

[4] K. N. Vijayasankar, D. Bonthu, M. Doddamani, F. Pati, *Mater. Today Commun.* **2022**, *33*, 104772.

[5] I. Polyakov, G. Vaganov, A. Didenko, E. Ivan'kova, E. Popova, Y. Nashchekina, V. Elokhovskiy, V. Svetlichnyi, V. Yudin, *Polymers* **2022**, *14*, 3803.

[6] N. P. Levenhagen, M. D. Dadmun, *Polymer* **2017**, *122*, 232.

[7] Y. Lyu, H. Zhao, X. Wen, L. Lin, A. K. Schlarb, X. Shi, *J. Appl. Polym. Sci.* **2021**, *138*, 1.

[8] M. J. Reich, A. L. Woern, N. G. Tanikella, J. M. Pearce, *Materials* **2019**, *12*, 1642.

[9] N. Vidakis, M. Petousis, E. Velidakis, N. Mountakis, P. E. Fischer-Griffiths, S. A. Grammatikos, L. Tzounis, *Polym. Test.* **2022**, *109*, 107545.

[10] M. Huang, Y. Xu, A. K. Schlarb, *J. Appl. Polym. Sci.* **2021**, *138*, 51409.

[11] I. L. Hay, A. Keller, *Kolloid-Zeitschrift Zeitschrift für Polym.* **1965**, *204*, 43.

[12] F. Zuo, J. K. Keum, X. Chen, B. S. Hsiao, H. Chen, S. Y. Lai, R. Wevers, J. Li, *Polymer* **2007**, *48*, 6867.

[13] R. Matsuzaki, N. Tsukamoto, J. Taniguchi, *Int. J. Adhes. Adhes.* **2016**, *68*, 124.

[14] H. Li, T. Wang, J. Sun, Z. Yu, *Rapid Prototyp. J.* **2018**, *24*, 80.

[15] C. McIlroy, P. D. Olmsted, *Polymer* **2017**, *123*, 376.

[16] J. Ghorbani, P. Koirala, Y. L. Shen, M. Tehrani, *J. Manuf. Process.* **2022**, *80*, 651.

[17] L. Wang, J. E. Sanders, D. J. Gardner, Y. Han, *Prog. Addit. Manuf.* **2018**, *3*, 205.

[18] N. P. Levenhagen, M. D. Dadmun, *Polymer* **2018**, *152*, 35.

[19] S. Charlon, J. Le Boterff, J. Soulestin, *Addit. Manuf.* **2021**, *38*, 101838.

[20] S. N. A. Majid, M. R. Alkahari, F. R. Ramli, S. Maidin, T. C. Fai, M. N. Sudin, *J. Mech. Eng.* **2017**, *2*, 185.

[21] J. R. Davidson, G. A. Appuhamillage, C. M. Thompson, W. Voit, R. A. Smaldone, *ACS Appl. Mater. Interfaces* **2016**, *8*, 16961.

[22] Y. Xu, M. Huang, A. K. Schlarb, *J. Appl. Polym. Sci.* **2022**, *139*, 52337.

[23] B. Suksut, A. K. Schlarb, *J. Appl. Polym. Sci.* **2016**, *133*, 1.

[24] L. Wang, W. M. Gramlich, D. J. Gardner, *Polymer* **2017**, *114*, 242.

[25] S. Hertle, M. Drexler, D. Drummer, *Macromol. Mater. Eng.* **2016**, *301*, 1482.

[26] C. McIlroy, R. S. Graham, *Addit. Manuf.* **2018**, *24*, 323.

[27] J. E. Seppala, S. Hoon Han, K. E. Hillgartner, C. S. Davis, K. B. Migler, *Soft Matter* **2017**, *13*, 6761.

[28] B. N. Turner, R. Strong, S. A. Gold, *Rapid Prototyp. J.* **2014**, *20*, 192.

[29] L. Lin, B. Suksut, A. K. Schlarb, in *Manufacturing of Nanocomposites with Engineering Plastics*, (Ed: V. Mittal), Woodhead Publishing, Germany **2015**, Ch. 12.

[30] J. Varga, G. W. Ehrenstein, A. K. Schlarb, *Express Polym. Lett.* **2008**, *2*, 148.

[31] R. M. Michell, A. Mugica, M. Zubitur, A. J. Muller, in *Advances in Polymer Science*, Vol. 276 (Eds: F. Auriemma, G. Alfonso, C. de Rosa), Springer, Cham, Spain **2017**.

[32] J. Kawabata, G. Matsuba, K. Nishida, R. Inoue, T. Kanaya, *J. Appl. Polym. Sci.* **1913**, *2011*, 122.

[33] C. McIlroy, P. D. Olmsted, *J. Rheol.* **2017**, *61*, 379.

[34] J. S. Mijovic, J. A. Koutsky, J. A. Koutsky, *Polym.-Plast. Technol. Eng.* **1997**, *9*, 139.

[35] S. Thanomchat, S. Kawee, S. Buncha, A. K. Schlarb, *Appl. Sci. Eng. Prog.* **2014**, *7*, 23.

SUPPORTING INFORMATION

Additional supporting information can be found online in the Supporting Information section at the end of this article.